A-Posteriori Error Estimation in CFD using Higher Moments

*S. Russant, D. Laurence, H. Iacovides, S. Utyuzhnikov

School of Mechanical, Aerospace and Civil Engineering, University of Manchester, UK

*Corresponding author: stuart.russant@postgrad.manchester.ac.uk

Abstract

Industry requires increases in CFD reliability while at the same time reductions in computational effort. A novel method for estimating both the shape and scale of solution errors from a single simulation is presented. The transport equation for a vector or scalar quantity and its second moment form are solved simultaneously. Information about the errors is contained in the difference between the two solutions, which is used to create an estimate in attempt to reconstruct the errors. The validity of this approach is established through the investigation of two test cases which have either an analytical or converged fine mesh solution. The error estimate successfully predicts the shape and scale of the real errors which is judged using two calculated values from each simulation. The shape prediction is evaluated using a correlation coefficient that ranged from -1 to 1. Error distributions with small features are impacted by inaccuracies in the process more than distributions with large features, leading to low (0.5 to 0.7) and high (0.8 to 1) correlation coefficients respectively. The scale prediction is judged by comparing averages of the distributions. There is a unique functional relationship between the averaged error estimate and the averaged real error. Therefore the error estimate, which is determined from numerical information generated on a single mesh, can be used to determine the magnitude of the numerical error of the simulation.

Contents

1 Introduction

Fluid flows and related phenomena can be described by partial differential equations, termed the governing equations (GE). These cannot be solved analytically except in special cases and so require the use of numerical methods to provide solutions. To obtain an approximate solution numerically a discretisation method must be applied to small domains in space and/or time. This approximates the differential equations by a system of algebraic equations so that the numerical solution provides results at discrete locations in space and time. But to find a solution to a complex fluid dynamics problem would generally require the repetitive manipulation of thousands, or even millions, of numbers ("degrees of freedom") which could not be achieved until creation of the high-speed digital computer. [Wendt (1992); Ferziger and Peric(2002)]

Once the power of computers had been recognised interest in numerical techniques increased dramatically. The increasing ability to simulate problems of more and more detail and sophistication was closely related to advances in computer hardware, particularly in regard to storage and execution speed which has been increasing according to Moore's Law since the 1950s. Solution of the equations of fluid mechanics on computers has become so important that it now occupies up to a third of all research into fluid mechanics and is still increasing. This field is known as computational fluid dynamics (CFD) and one of the strongest forces driving the development of new supercomputers is coming from the CFD community. [Rouse et al. (1957)]

Roache (1998) noted that "the problem caused by the rapid development of computers was that the universe of possible problems is so extensive, and the power of simulations so great, that CFD practitioners often focused on qualitative simulation of the next more difficult problem class that the computer capabilities just barely allowed, rather than on achieving quantitative accuracy on the previous problem class," commenting that sometimes this has led to a decrease in the quality of simulations published. As an improvement to standards, the ASME Journal of Fluids and Engineering stopped accepting papers reporting numerical fluid engineering solutions that fail to address the task of systematic truncation error testing and accuracy estimation, making it clear that it is not possible to infer an accuracy estimate from a single calculation on a fixed grid. This paper sets out to challenge this by investigating a method to estimate solution errors from a single simulation.

Today there is world-wide and general interest for quantifying errors and uncertainties in CFD studies, for example in industrial design, across industry sectors but particularly safety applications where demand for "error bars" around CFD results is now pressing. Before we can address these issues, error and uncertainty need to be distinguished. From [AIAA (1998)]

- An error is defined as "a recognisable deficiency in any phase or activity of modelling and simulation that is not due to lack of knowledge," implying that the deficiency is identifiable upon examination. According to the Best Practice Guidelines [Casey and Wintergerste (2000)] an example would be numerical errors which result from the differences between the solutions of the exact equations and the discretised equations solved by the CFD code. These would include: Spatial or temporal discretisation errors where replacing the analytical derivatives or integrals in the exact governing equations by numerical approximations involves introducing a truncation error; iteration error caused by the premature ending of a simulation of a steady state flow problem using an iterative method before the steady-state solution is found; round off errors resulting from the fact that a computer only solves the equations with a finite number of digits.
- An uncertainty is defined as "a potential deficiency in any phase or activity of the modelling process that is due to the lack of knowledge," indicating that deficiencies may or may not exist. This would mostly be the result of a lack of knowledge about the physical processes that go into building a model, for example the uncertainties that arise from deficiencies in turbulence modelling since there is a lot about turbulence modelling that is not yet understood.

Blottner (1997) distinguishes two distinct reasons error and uncertainty are introduced into simulations. These come from either inappropriate governing equations or inaccurate numerical solution procedure, which are systematically identified and reduced through validation and verification methods respectively. [AIAA (1998)] defines validation as: "The process of determining the degree to which a model is an accurate representation of the real world from the perspective of the intended uses of the model," and verification as

"The process of determining that a model implementation accurately represents the developer's conceptual description of the model and the solution to the model." These methods require time to be spent on further investigation, time which in industrial applications is monetarily expensive. Therefore such in-depth error analysis may be overlooked, leading to unreliable results.

This paper focusses on verification of numerical errors. After a brief introduction of the governing equations of CFD in the finite volume method the paper presents the second moment solution estimate (SMSE). This is an error estimate, and by definition is expected to give information about both the location and size of the simulation errors. The creation of this error estimate aims to address the previously mentioned concerns. This is done by producing an estimate using only one run and one grid allowing quick, inexpensive error analysis. This will thereby increase reliability of results without significantly increasing the computational effort or time required. [Casey and Wintergerste (2000)] The method is tested against two complex test cases with the transport of a passive scalar using a constant flux or constant value boundary condition.

2 Governing Equations of CFD in the Finite Volume method

Following the descriptions in [Wendt (1992); Ferziger and Peric(2002)], the governing equations of CFD derive from the basic conservation laws of mass, momentum and energy:

1) The mass of a fluid is conserved as mass cannot be created or destroyed.

2) The rate of change of momentum equals the sum of the forces on a fluid particle (Newton's second law).

3) The rate of change of energy is equal to the sum of the rate of heat addition to the rate of work done on a fluid particle (first law of thermodynamics).

These fundamental principles can be expressed as mathematical statements, typically partial differential equations. The fluid is treated as a continuum, and considers the flow of a control mass (CM) within a certain spatial region called a control volume (CV). A CM has associated with it extensive properties such as mass, momentum and energy, while a CV has associated with it intensive properties such as mass or momentum per unit volume.

For conserved intensive property ϕ of the CM with volume Ω_{CM}, density ρ and velocity field $\mathbf{u}$, the corresponding extensive property Φ is found from the control volume equation for the CV

$$\Phi = \int_{\Omega_{CM}} \rho\phi \mathrm{d}\Omega \tag{1}$$

A conservation equation governs the rate of change of the extensive property

$$\frac{\mathrm{d}\Phi}{\mathrm{d}t} = \Gamma$$

where Γ is all other contributions to Φ. The left hand side (LHS) of the conservation equation therefore yields:

$$\frac{\mathrm{d}}{\mathrm{d}t}\int_{\Omega_{CM}} \rho\phi d\Omega = \frac{\partial}{\partial t}\int_{\Omega_{CV}} \rho\phi d\Omega + \int_{A_{CV}} \rho\phi \mathbf{u}\cdot\mathbf{n} dA \tag{2}$$

with CV volume Ω_{CV} and surface A_{CV}. Equation 2 states that the rate of change of the amount of the property in the control mass, Φ, is the rate of change of the property within the control volume plus the net flux of it through the CV boundary due to fluid motion relative to the CV boundary. The first term is time dependent and is named the 'transient'. The second term is called the convective term and represents the convective flux of ϕ through the CV boundary. More detailed derivations of this equation can be found in [Bird et al (1962); Fox and McDonald (1982)]

2.1 *Mass*

For mass $\phi = 1$ and without the mass source term, Γ, the right hand side of the conservation equation is zero, leading to

$$\frac{\mathrm{d}}{\mathrm{d}t}\int_{\Omega} \rho \mathrm{d}\Omega + \int_{A} \rho \mathbf{u} \cdot \mathbf{n} dA = 0 \tag{3}$$

where Ω and A are now the volume and surface of the CV. Using the divergence theorem and allowing the control volume to become infinitesimal leads to:

$$\frac{\partial \rho}{\partial t} + \nabla \cdot \rho \mathbf{u} = 0 \tag{4}$$

For incompressible flow this becomes

$$\nabla \cdot \rho \mathbf{u} = 0 \tag{5}$$

Equation 4 can also be used to re-write the term $\frac{\partial \rho \phi}{\partial t}$ as follows:

$$\rho \frac{\partial \phi}{\partial t} - \phi \nabla \cdot \rho \mathbf{u} \tag{6}$$

2.2 *Momentum*

For momentum $\phi = \mathbf{u}$, and the right hand side of the conservation equation is equal to the sum of the forces, $\mathbf{f}$, acting on the fluid particle, leading to

$$\frac{\mathrm{d}}{\mathrm{d}t}\int_{\Omega} \rho \mathbf{u} \mathrm{d}\Omega + \int_{A} \rho \mathbf{u}\mathbf{u} \cdot \mathbf{n} \mathrm{d}A = \sum \mathbf{f} \tag{7}$$

With no other forces acting other than viscous forces, turbulent stresses σ, and body forces $\mathbf{b}$, and again using the divergence theorem and allowing the control volume to become infinitesimally small, in non conservative form this becomes

$$\frac{\partial (\rho \mathbf{u})}{\partial t} + \nabla \cdot (\rho \mathbf{u}\mathbf{u}) = \nabla \cdot \sigma + \rho \mathbf{b} \tag{8}$$

The stress tensor σ for Newtonian fluids and laminar flow is

$$\sigma = \tau - P\mathbf{I} \tag{9}$$

where P is the pressure, $\mathbf{I}$ is the identity matrix and τ is the viscous stress tensor defined from the dynamic molecular viscosity, $\mu = \mu_l$, and the strain rate tensor $\mathbf{D}$ as:

$$\tau = 2\mu \mathbf{D} - \frac{2}{3}\nabla \cdot \mathbf{u}\mathbf{I} \tag{10}$$

with

$$\mathbf{D} = \frac{1}{2}(\nabla \mathbf{u} + (\nabla \mathbf{u})^T) \tag{11}$$

With the stress tensor known, and in conservative form using equation 5 the momentum conservation equation becomes

$$\frac{\partial \mathbf{u}}{\partial t} + \mathbf{u} \cdot \nabla \mathbf{u} = \frac{\mu}{\rho}\nabla^2 \mathbf{u} - \frac{\nabla P}{\rho} + \mathbf{b} \tag{12}$$

2.3 *Advection of a Scalar*

From equation 7, using equation 6 and using Fick's law with diffusivity β to separate the diffusive source term from other additional source terms, S_i, the advection of a scalar f (such as enthalpy, temperature, concentrations or mass fractions) becomes:

$$\frac{\mathrm{d}}{\mathrm{d}t}\int_{\Omega}\rho f \mathrm{d}\Omega + \int_{A}\rho f \mathbf{u}\cdot\mathbf{n}\mathrm{d}A = \int_{A}\beta\nabla f\cdot\mathbf{n}\mathrm{d}A + \int_{\Omega} S\mathrm{d}\Omega \tag{13}$$

becoUsing the divergence theorem, equation 5, and allowing the control volume to become infinitesimal, equation 13 becomes:

$$\frac{\partial f}{\partial t} + \mathbf{u}\cdot\nabla f = \nu\nabla^2 f + S \tag{14}$$

where $\nu = \frac{\beta}{\rho}$ and S has been redfined to include the division by ρ. This paper reports on error estimation for solutions to the scalar transport equation. The error will be the difference between the the solution of this equation, f, and the exact solution, f_e. In this paper the real error will be defined as

$$\delta = f - f_e \tag{15}$$

3 Second Moment Solution Method

This section introduces the second moment equation (SME). This is a higher moment of the scalar transport equation and is itself a transport equation, but one for the scalar squared. The proposed method obtains a solution to the SME at the same time as the main calculation for the velocity and scalar. By doing this, the simulation will solve equations for both a variable and the variable squared. The question this paper investigates is whether additional information can be found using the squared-variable solution of this second equation (i.e. by comparisons with the unsquared-variable solution). The inspiration for this comes from the calculation of the variance of a variable, x:

$$\mathrm{Var}(x) = \langle x\rangle^2 - \langle x^2\rangle \tag{16}$$

where variations in the data are revealed by comparing the mean of x squared and the mean of x^2. Through the squaring process the differences were exaggerated so that the two terms are not identical and so a measure of the deviation is found. Similarly this effect is expected when solving the SME for the squared-variables. It will be shown later exactly how comparisons between the two solutions will depend on the unsquared-variable solution errors.

3.1 *Manipulation of the Scalar Transport Equation into the Second Moment*

Starting with the simpler case of scalar transport, the transformation into the second moment begins by multiplying the steady, Cartesian form of Equation 14 by f [Jasak (1996)] to get

$$f\mathbf{u}\cdot\nabla f - \beta f\nabla^2 f = fS \tag{17}$$

When rearranged, it produces a similar equation, this time representing the transport of $q\left(=\frac{f^2}{2}\right)$:

$$\mathbf{u}\cdot\nabla q - \beta\nabla^2 q = fS - \beta\nabla f\cdot\nabla f \tag{18}$$

where the relations $\nabla f^2 = 2f\nabla f$ and $\nabla^2 f^2 = 2f\nabla^2 f + 2\nabla f\cdot\nabla f$ have been used.

From the point of view of a numerical solver this is exactly the same as solving Equation 14, where f in the LHS of the equation has been replaced by a variable $q\left(=\frac{f^2}{2}\right)$, and with the addition of an extra source term $fS - \beta\nabla f\cdot\nabla f$. This equation for q is termed the second moment, and the original equation for f will be referred to as the first moment. This second moment was used by [Jasak (2010)] to calculate a residual for each cell using the solution to the first moment, which, after rescaling, became an error estimate.

3.2 *Solving the Second Moment Equations (SME)*

The second moment equation can be solved for q by any CFD software, such as the EDF open source code, *Code_Saturne*, used in this study. For the solver this is the same as solving any scalar transport equation. The one difference is that the source term on the RHS of the SME requires information about the first moment exact solution f_e, which is unknown. The SME cannot be solved using the CFD solver without knowledge of the distribution of f_e and so the source must be obtained from the numerical solution for f on the same mesh. While the first moment is solved iteratively to find f, the gradients of the current distribution of f are calculated each iteration. These are used as input into the solver as the source term for the SME according to Equation 18 and is simultaneously solved.

The process therefore introduces error into the calculation of q. Two additional errors are introduced into the SME calculation this way: First f will have their own associated errors and so their gradients will differ from the exact gradients; second the calculation of the gradients will have truncation errors in the discretisation process. These will be transferred to the SME through an incorrect source term and will affect the solution. In this paper these q errors will be defined as

$$\varepsilon = q - q_e \tag{19}$$

The result of this is that although the exact solutions obey the relation $q_e = \frac{f_e^2}{2}$, the simulation solutions do not obey $q = \frac{f^2}{2}$. This is what will be exploited to reveal additional information about the real errors to create an error estimate.

3.3 *Combining the Solutions of the First and Second Moments*

Any direct comparison of the two solutions should leave a residual because the numerical solutions do not obey the relation $q = \frac{f^2}{2}$. There are two combinations of the numerical solutions that provide information of interest to the current efforts. The first is used to gain an estimate of the shape of the real error:

$$q - \frac{f^2}{2} \tag{20}$$

This has the units of f^2 which is incompatible with estimates of the errors, which have the units of f. Therefore rescaling to the correct units is required. Using Equations 15 and 19 it is possible to break this combination down into contributions from the errors from the two solutions

$$q - \frac{f^2}{2} = \varepsilon - \delta f + \frac{\delta^2}{2} \tag{21}$$

The derivation for this is shown in Appendix A. Now it can be seen what makes up this combination, and why it is expected to be a good estimation of the shape. It is reasonable to expect the q error, ε, and $\frac{\delta^2}{2}$, to be in some way similar in shape to the f error. So these two terms will contribute to a good estimation of the shape. The remaining term δf will not contribute to a good estimate of the shape because multiplication by f will distort it, creating a higher relative prediction of error in regions of high f.

The second combination, which is used to estimate the scale of the real error, is:

$$f - \sqrt{2q} \tag{22}$$

This has the units of f and is used to rescale the previous combination. Again using Equations 15 and 19 it is possible to break this down into contributions from the errors from the two solutions

$$f - \sqrt{2q} \approx \delta - \frac{\varepsilon}{2f_e} \tag{23}$$

The derivation for this is shown in Appendix A. Now it can be seen what makes up this combination and why it should be a good estimation of the scale. The first term δ is the value the estimate is trying to reproduce. The second term $\frac{\varepsilon}{2f_e}$ will be a very different shape to δ due to the division by f_e, but will be within the same order as δ and not the same. This means that this combination cannot be used to predict the shape, but can be used to get a number that is of the same order as the real error. A typical value of this will be used to rescale the previous shape combination.

3.4 *Scalar Error Estimate*

The two comparisons described are theoretically capable of reproducing the shape or scale of the f simulation error. The two need to be combined so that a single output can be produced for analysis by the CFD user. The proposal is to rescale the better estimation of the shape with the better estimation of the scale, but there are different ways to acquire a typical value from the distributions. One example would be the maximum values, however, in this work it will be the volume average of a distribution that is used. For the rescaling these averages need to be a typical value of what is actually there, so a cut off was used to exclude the large regions of zero value that appear in the distributions. The exclusion chosen was all cells with a value lower than 5% of the range between the maximum and the minimum value of the distribution, i.e. for a distribution of $\left|q-\frac{f^2}{2}\right|$, all cells with value less than $\min\left(\left|q-\frac{f^2}{2}\right|\right)+0.05\left[\max\left(\left|q-\frac{f^2}{2}\right|\right)-\min\left(\left|q-\frac{f^2}{2}\right|\right)\right]$ are excluded from the average. The rescaling is done by dividing by the excluded average of the shape estimate and multiplying by the average of the scale estimate.

Next the estimate is expressed as a percentage of a typical value of the f solution. Again it will be found using a volume average, however, there will be no exclusion in calculating this average f, with the intention of transferring information about the Reynolds number into the estimate. A final rescaling includes a factor of two and this is justified in Appendix B. If the error estimate is defined as ξ, then

$$\xi = 2\frac{\left|q-\frac{f^2}{2}\right|\cdot \text{average}_{>5\%}\left(\left|\sqrt{2q}-f\right|\right)}{\text{average}_{>5\%}\left(\left|q-\frac{f^2}{2}\right|\right)}\frac{100\%}{\text{average}\left(|f|\right)} \tag{24}$$

where $\text{average}_{>5\%}$ indicates the volume average with a 5% exclusion.

4 Error Estimate Evaluation Coefficients

4.1 *Summation Coefficient to Compare the Scale of the Error Estimate*

The error estimate may have superficial differences in shape that do not match the real error. These would be caused by the unusual combination of the f and q errors that results from the $q-\frac{f^2}{2}$ shape estimate. The values of the error and estimate at certain points could be taken from the results as a way to compare them. However, this can lead to misleading results if the shape is warped in some way, for example the location of the peaks is transposed slightly. Instead, to compare the scale prediction a summation of the values of each over all of the cells was considered. This was done to reduce the effect of any local skewing. Many of the cells in the following test case results will be near to zero and therefore an exclusion was used. It was chosen to be 5% of the range between the maximum and minimum error or estimate on the grid, the same as described in the previous section. To allow comparison, the real error was made into a percentage using the unexcluded average f value used in the previous section with the estimate. The error and estimate summation coefficients are

$$\text{Error Summation} = \sum_{|f-f_e|>\min(|f-f_e|)+0.05\left[\max(|f-f_e|)-\min(|f-f_e|)\right]} \frac{|f-f_e|}{\max(f)}\cdot\frac{V_{cell}}{V_{total}}\cdot 100\% \tag{25}$$

$$\text{Estimate Summation} = \sum_{|\xi|>\min(|\xi|)+0.05\left[\max(|\xi|)-\min(|\xi|)\right]} \xi\cdot\frac{V_{cell}}{V_{total}} \tag{26}$$

4.2 *Cross Correlation Coefficient to Compare the Shape of the Error Estimate*

It is possible that the error estimate predicts the scale of the real error poorly, while at the same time the shape is predicted well. A way to compare the shapes of the error and the estimate separate from the scale is therefore required. A single number to compare the correlation between the two is needed, similar to the summation coefficients. An image comparison technique was used to compare the two. The chosen technique will be the normalised cross correlation coefficient [Lemieux and Barker (1998)] because it assumes there is a linear relationship between the two compared images rather than simple Gaussian noise. The correlation coefficient *NCC* between the real error distribution δ and the error estimate ξ is defined as

$$NCC = \frac{1}{n}\sum \frac{\left(\delta_i - \bar{\delta}\right) \cdot \left(\xi_i - \bar{\xi}\right)}{\sigma_\delta \sigma_\xi} \tag{27}$$

where n is the number of cells, $\bar{\delta}$ and $\bar{\xi}$ are the average across the errors and the estimates, σ_δ and σ_ξ are the standard deviations of the error and the estimate respectively. The coefficient ranges from -1 to 1, with a value of 1 occuring when there is perfect correlation between the two distributions. A high correlation is found when the distributions both have peaks and minima in the same locations. Low correlations are found when one of the distributions has peaks where the other has minima. The correlation coefficient is not affected by addition or multiplication to either of the distributions and is only affected where the peaks and minima are and their relative heights. This means that if the scale is not predicted correctly the correlation can still be studied between the simulations. Comparisons using the correlation coefficients is most informative when comparing between similar simulations, it is not necessarily reliable to compare between two different simulations.

5 Test cases

The two test cases investigated focus on the scalar transport of a passive scalar across a 'hot' wall into the fully developed fluid flow moving over it. The scalar will be introduced by one of the boundaries being set to have either constant flux or constant value of the scalar f. All other boundaries will have the value and flux of the scalar equal to zero. If the constant flux boundary has a flux of f equal to j, the same boundary condition is used for the q simulation and the flux is equal to $j\frac{\partial f}{\partial x_i}$, where x_i is the normal to the wall. If the constant value boundary has a value m, then the same boundary condition is used for the q simulation and the value is equal to $\frac{m^2}{2}$. At the inlet both f and q are equal to zero so that it is the relative change in the scalar that is seen.

Five Reynolds numbers (*Re*) were used for each test case which ranged from laminar *Re* to above the turbulent transition *Re*. The simulations reported here are for laminar simulations only, no turbulence model was used even though the *Re* becomes high enough to require one.

In both test cases three refinements of meshes were used. A refined mesh is used to produce a converged solution f_e. This was done because there was no analytical solution for these flows and this is serves as the 'gold standard' solution free of numerical error. The other two meshes were a coarse and very coarse mesh, and were made coarse enough to generate errors of numerical significance; above 10% of the typical value of the f distribution. On these two meshes the first and second moment equations are solved for f and q respectively. The simulation errors were calculated by the local cell difference between the refined mesh solution f_e and one of the coarser mesh solutions.

The CFD solver used is the open source software *Code_Saturne* version 2.0.1 and the simulations will use three discretisation schemes: first order upwind (FO), second order centred (SO) and second order linear upwind (SOLU). This means there are thirty simulations in total for this flow case.

5.1 *Heated Ribbed Channel Flow*

The first test case examines the situation of a scalar transport inside a laminar flow along a ribbed channel. The flow geometry is a 2D channel with small square regularly spaced protrusions sticking out of one wall, which are the ribs. The ribs are a tenth of the channel width and their spacing is the same as the channel width. A diagram of this is shown in Figure 1. The flow presents complications to finding CFD solutions of the flow due to the corners of the ribs. These cause singularities in the flow - resolving the mesh finer in these areas will change the flow solution. The simulation is the scalar transport of a passive scalar from the lower 'hot' walls into the fully developed fluid flow.

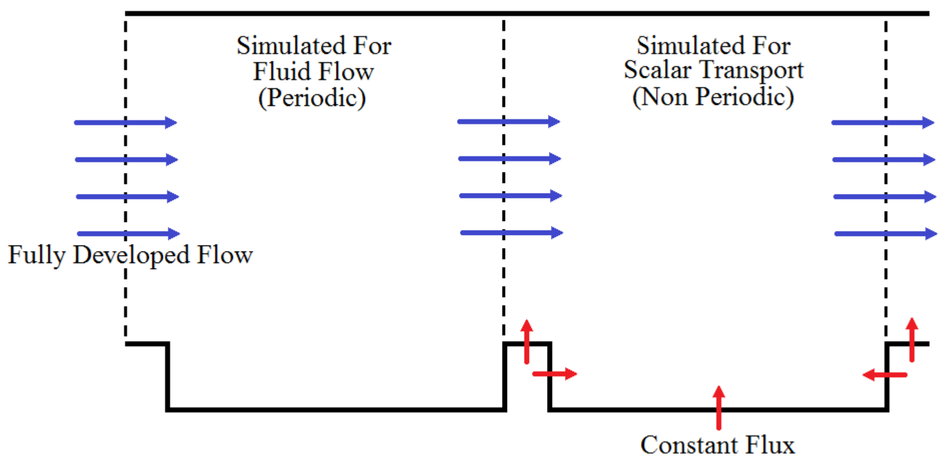

Figure 1: A diagram of the ribbed channel geometry indicating the direction of flow and scalar flux.

The range of Reynolds number used was $Re = 350$, 700, 1050, 1400, and 1750. The very coarse mesh had 25 cells along the length of the channel and 2 cells up the side of the rib. The coarse mesh had 50 cells along the length of the channel and 5 cells up the side of the rib. The flow solution will be found in a periodic simulation, representing the fully established flow in a long ribbed channel. The flux boundary condition of the scalar f along the lower wall and the rib walls was a constant $0.1[f]\mathrm{m}^{-1}$ into the fluid. The value boundary condition of the scalar f along the lower wall and the rib walls was a constant $10[f]$. The test case requires finding a converged solution to the flow first to be used as a frozen velocity in a non periodic simulation for the scalar transport. This is necessary because the scalar transport will not reach a steady state in the periodic simulation. The investigation simulates the transport of a passive scalar into this fully developed flow as if the first 'hot' section of ribs were just being encountered.

5.1.1 *Velocity Solution*

The flow found for the refined mesh simulation with $Re = 350$ and 1400 is shown in Figure 2 for the lower half of the geometry. There is a recirculation region after the first rib and it increases in size as the Reynolds number increases. In each there is also a much smaller recirculation region in the downstream rib corner which also increases in size with Reynolds number.

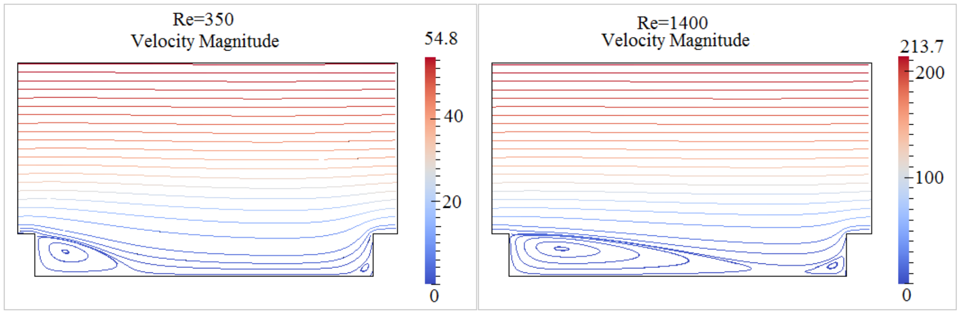

Figure 2: Velocity stream lines found with the fine mesh for $Re = 350$ (left), and $Re = 1400$ (right).

5.1.2 *Solving for f*

Examples of the f distribution are shown in Figure 3 for both boundary condition types. With the constant flux boundary condition the regions of high f are in the corners shadowed by the ribs. The wall value is not fixed so there will be error along it. The gradient will be shallow compared to the constant value boundary solution because the maximum value is small. With the constant value boundary condition the entire region in between the ribs has a high f value. The fixed wall value forces the f solution to a higher number than the constant flux result. The error at the wall will be zero but the gradient of f will be higher.

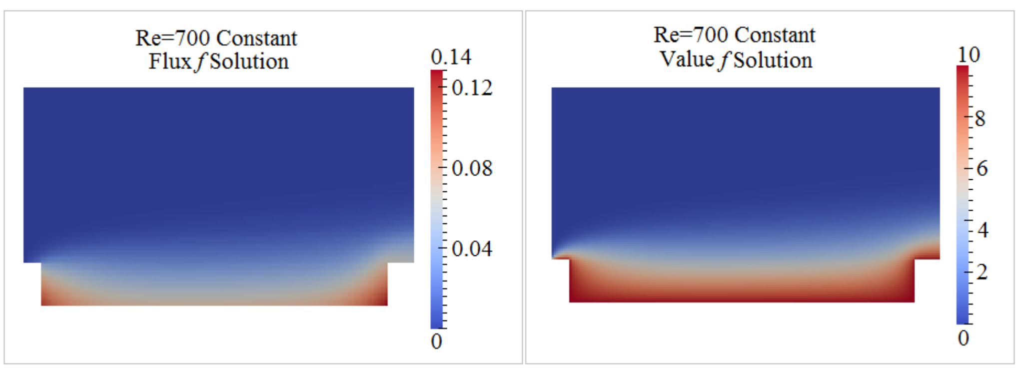

Figure 3: The refined mesh f solutions for $Re = 700$. Left is the constant flux boundary result, right is the constant value boundary result.

5.2 *Impinging Flow*

This test case investigates the situation of 2D flow through a pipe that impinges onto a perpendicular pipe, splitting the flow. Figure 4 shows a diagram of the geometry. The geometry is an inlet channel long enough to set up developed flow that then meets a perpendicular pipe of the same thickness. This creates an impingement on the back wall, which is the source of the passive scalar f. The impingement point in this flow, labelled A in Figure 4, is a singularity and so it should be able to generate significant errors in the simulation.

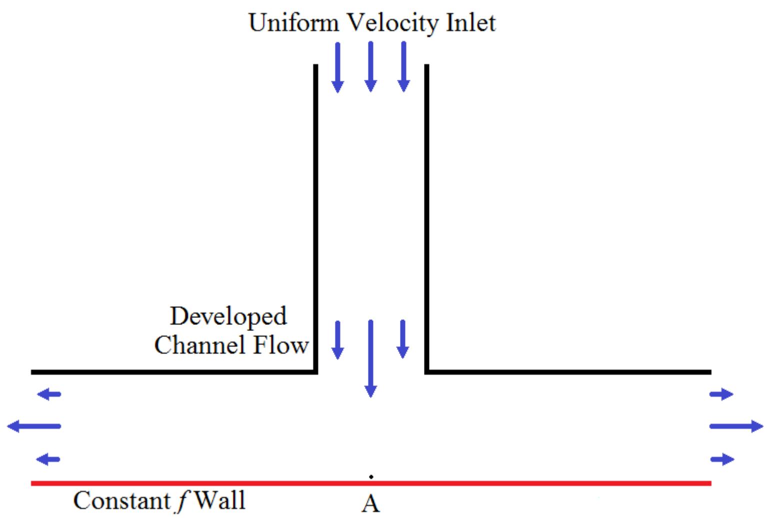

Figure 4: The geometry of the 2D impinging flow test case. A - $x = 0$, the impingement point.

The inlet condition for the velocity was constant speed into the pipe and was adjusted to create five Reynolds numbers for the investigation. These were $Re = 500$, 1000, 1500, 2000, and 2500. The very coarse mesh had eight cells across the channel while the coarse mesh had sixteen cells. The flux boundary condition of the scalar f along the lower wall and the rib walls was a constant $100[f]\mathrm{m}^{-1}$ into the fluid. The value boundary condition of the scalar f along the impingement wall was a constant $10[f]$.

5.2.1 *Velocity Solution*

The flow solution for the refined mesh solution is shown in Figure 5. The inlet channel was long enough for the flow to become fully developed. The flow enters the horizontal pipe and hits the back wall, splitting it at the impingement point. The flow then moves down the side channels and returns to a developed channel flow.

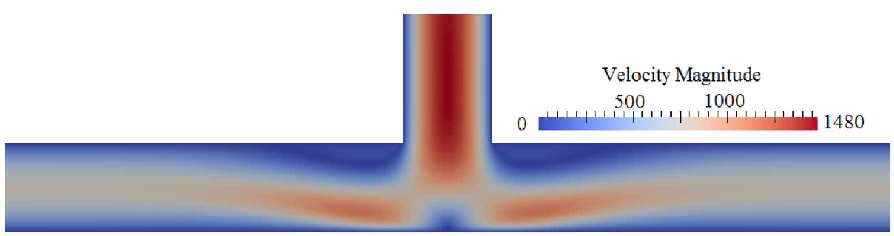

Figure 5: The velocity solution for the impinging flow test case with $Re = 1000$.

5.2.2 *Solving for f and q*

Figure 6 shows the refined mesh f distribution for half the geometry, with $Re = 1000$ for both boundary condition types. With the constant flux boundary condition the impingement point has a region of low f value. Downstream it builds up, leading to high values near the wall. With the constant value boundary condition a similar effect is seen, but close to the wall it remains at a high value of f leading to a higher gradient close to the wall at the impingement point.

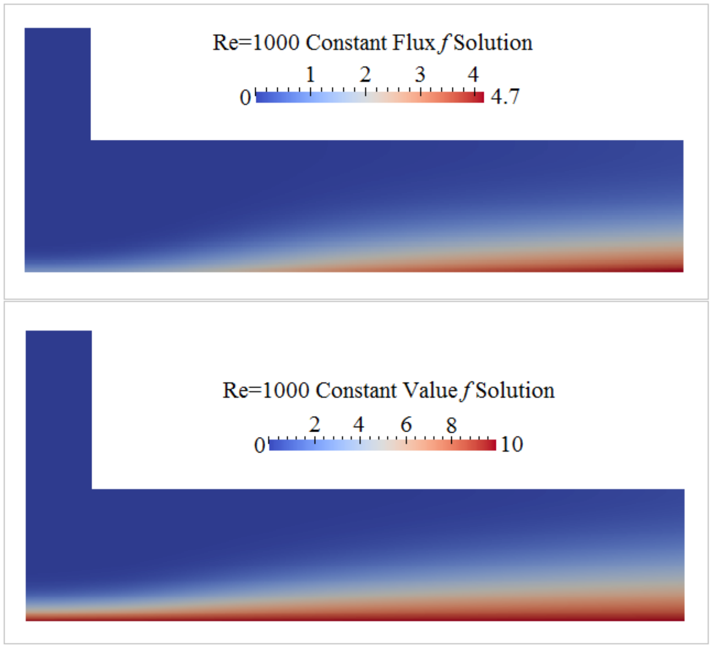

Figure 6: The f solution found using the fine mesh with $Re = 1000$ and a constant flux boundary along the bottom wall (top) and constant value (bottom).

6 Results

A good error estimate requires that both the shape and the scale are predicted well. This section will compare the error estimate distributions to the real error distributions using the two calculated values described in the method section.

6.1 *Shape Prediction with Correlation Coefficients*

How well the shape has been predicted is judged by the correlation coefficient. In Figure 7 the correlation coefficients are shown for the different simulations. They are plotted as coefficient against discretisation scheme and mesh refinement. The following sections will discuss the four graphs and present unscaled colour maps for shape comparison only.

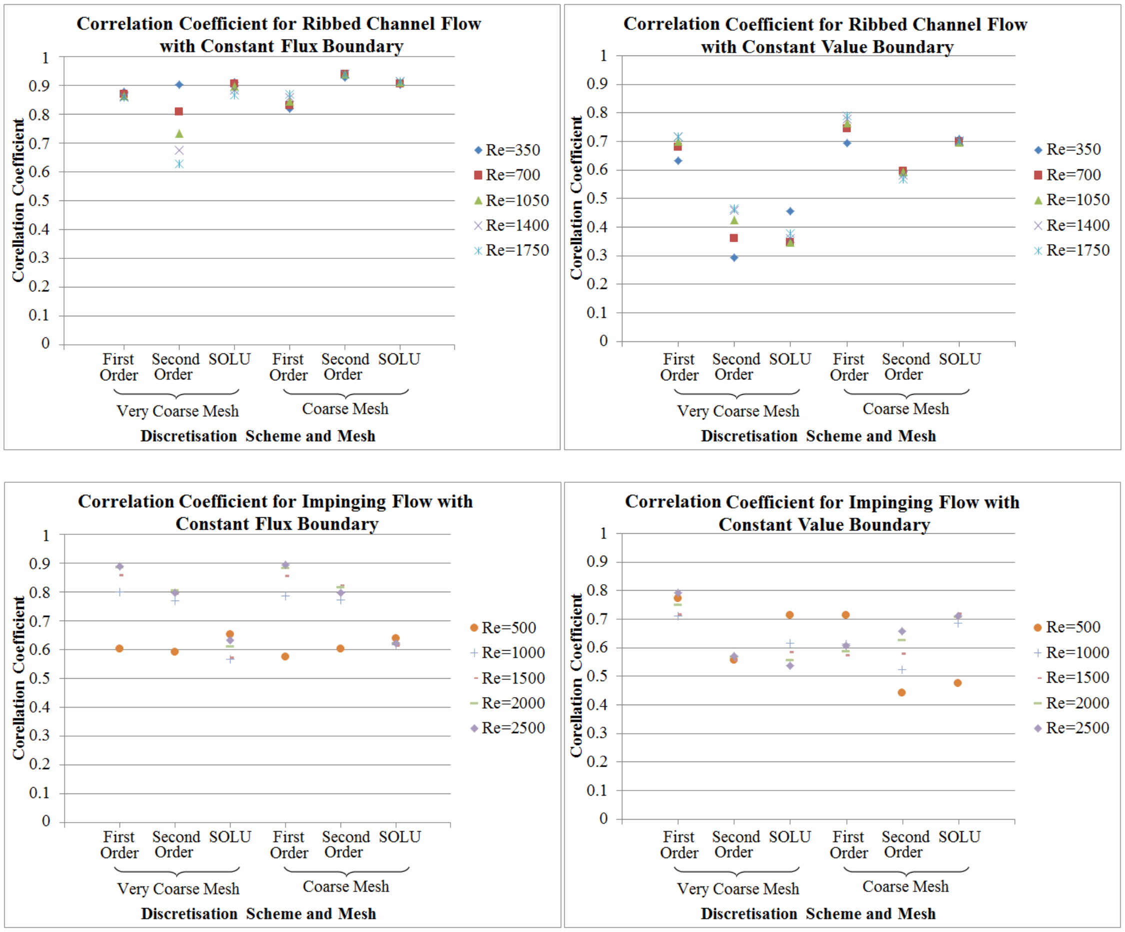

Figure 7: Correlation coefficients plotted against the discretisation scheme and mesh refinement for the five *Re*. The top graphs are the ribbed channel with constant flux boundary (left) and constant value boundary (right). The bottom graphs are impinging flow with constant flux boundary (left) and constant value boundary (right).

6.1.1 *Ribbed Channel with Constant Flux Boundary*

Figure 8 shows two examples of the error and estimate distribution. The first is for the coarse mesh with the second order centred scheme at $Re = 700$, which produced the highest correlation coefficient of 0.94. The second is for the very coarse mesh with the second order centred scheme at $Re = 1750$, which produced the lowest correlation coefficient of 0.63. The top left graph in Figure 7 shows that the correlation coefficients were generally high between 0.8 and 0.9, and appear to be visually similar. The exception is for the results on the very coarse mesh with the second order centred scheme; the correlation coefficient becomes worse with increasing *Re*.

In the region near the downstream rib in the $Re = 1750$ simulation with the very coarse mesh, there is a relative over prediction. This is typical of the error estimates that produce low correlation coefficients in this test case and with the constant flux boundary condition. The explanation for this is that the cell Peclet number increases to a point where unboundedness becomes an issue for the centred scheme. In this region the cell Peclet number was as high as 15; high enough to have caused an effect. With the coarse mesh the cell Peclet number in this region was 7.5 and so less of an effect was seen.

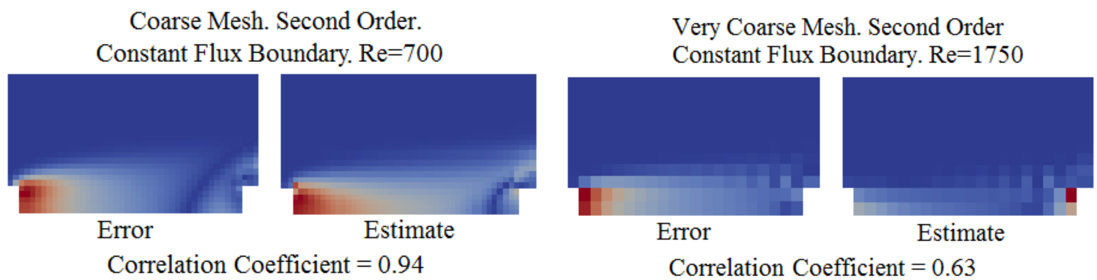

Figure 8: Distributions of real error and error estimate for simulations where the correlation coefficient has been high (left) and low (right).

6.1.2 *Ribbed Channel with Constant Value Boundary*

Figure 9 shows two examples of the error and estimate distribution. The first is for the coarse mesh with the first order scheme at $Re = 1750$, which produced the highest correlation coefficient of 0.79. The second is for the very coarse mesh with the second order centred scheme at $Re = 350$, which produced the lowest correlation coefficient of 0.29. The correlation coefficients were lower for the constant value boundary than for the constant flux. This is because the features in the real error distributions are in general small sharp peaks and in this situation even slight variations in the error estimate distributions can lead to a large drop in coefficient.

The first order results varied from 0.7 to 0.8 and both of the second order results varied from 0.3 to 0.7. This will partly be caused by the high Peclet numbers in some of the simulations as seen before. Figure 9 reveals the second reason in the error estimate distribution. The first cells along the 'hot' boundary do not go to zero. The result is unexpected because the real error would be zero next at the constant value boundary. This effect was observed in all second order simulations but not in the first order. The cause of this is attributed to a combination of the high Peclet number as well as the decreased order of gradient estimation near the wall.

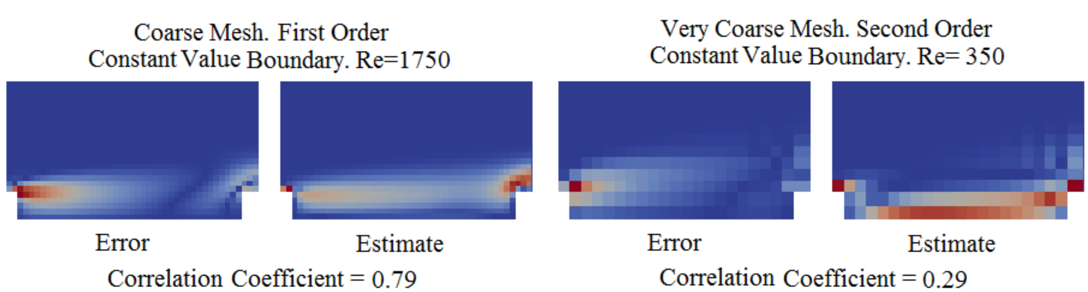

Figure 9: Distributions of real error and error estimate for simulations where the correlation coefficient has been high (left) and low (right).

6.1.3 *Impinging Flow with Constant Flux Boundary*

Figure 10 shows two examples of the error and estimate distribution. The first is for the coarse mesh with the first order scheme at $Re = 2500$, which produced the highest correlation coefficient of 0.89. The second is for the very coarse mesh with the second order linear upwind scheme at $Re = 1000$, which produced the lowest correlation coefficient of 0.57. In the error estimates there is a band of zero estimate cutting through the distribution, demonstrated in the high correlation example in Figure 10. This is caused by taking the absolute values of a distributions whose real values change sign. Although the values are zero in such regions, it should be noted that this region has a high gradient error/estimate.

In Figure 10 (right) the most prominent feature is the peak of error, and in the error estimate this feature is seen a few cells away. The effect of this would be to reduce the correlation coefficient. This occured in a number of the low correlation coefficient simulations, including the $Re = 500$ simulations, and in Figure 7 it can be seen that for $Re = 500$ the correlation coefficients are much lower compared to the other simulations.

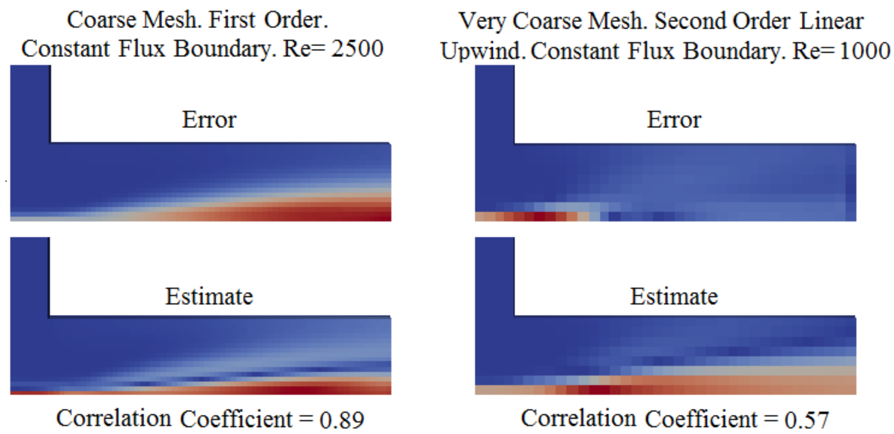

Figure 10: Distributions of real error and error estimate for simulations where the correlation coefficient has been high (left) and low (right).

6.1.4 *Impinging Flow with Constant Value Boundary*

Figure 11 shows two examples of the error and estimate distribution. The first is for the coarse mesh with the first order scheme at $Re = 2500$, which produced the highest correlation coefficient of 0.79. The second is for the very coarse mesh with the second order centred scheme at $Re = 500$, which produced the lowest correlation coefficient of 0.44. The first order results appear to have produced a better shape prediction than the second order, the error estimate is almost identical to the real error. Again for the second order results the first row of cells along the heated boundary are unexpectedly high. In the example shown it appears those first high in value cells are masking a distribution that is quite similar to the real error. This problem affects all of the second order results and not the first order.

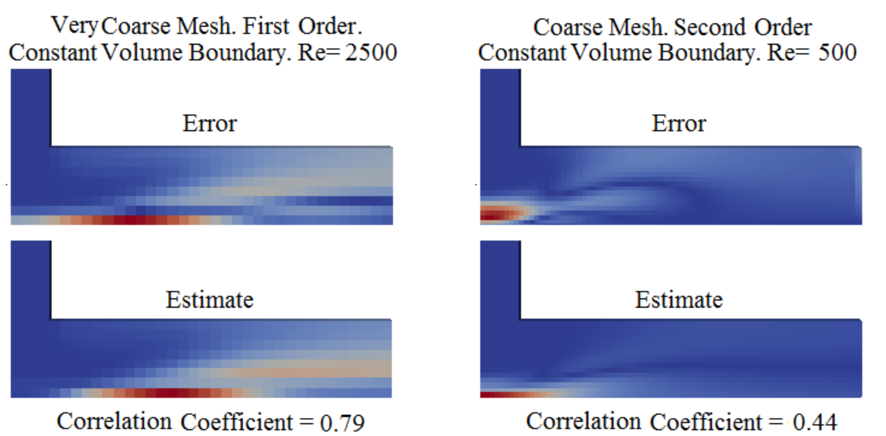

Figure 11: Distributions of real error and error estimate for simulations where the correlation coefficient has been high (left) and low (right).

6.2 *Scale prediction*

How well the scale has been predicted is judged by the summation coefficients. In Figure 12 these have been plotted as summation error divided by estimate against summation estimate. Results with the same discretisation scheme and mesh refinement are joined by lines. This shows the effect of changing the Reynolds number on a certain set up, and there appears to be a clear relationship emerging.

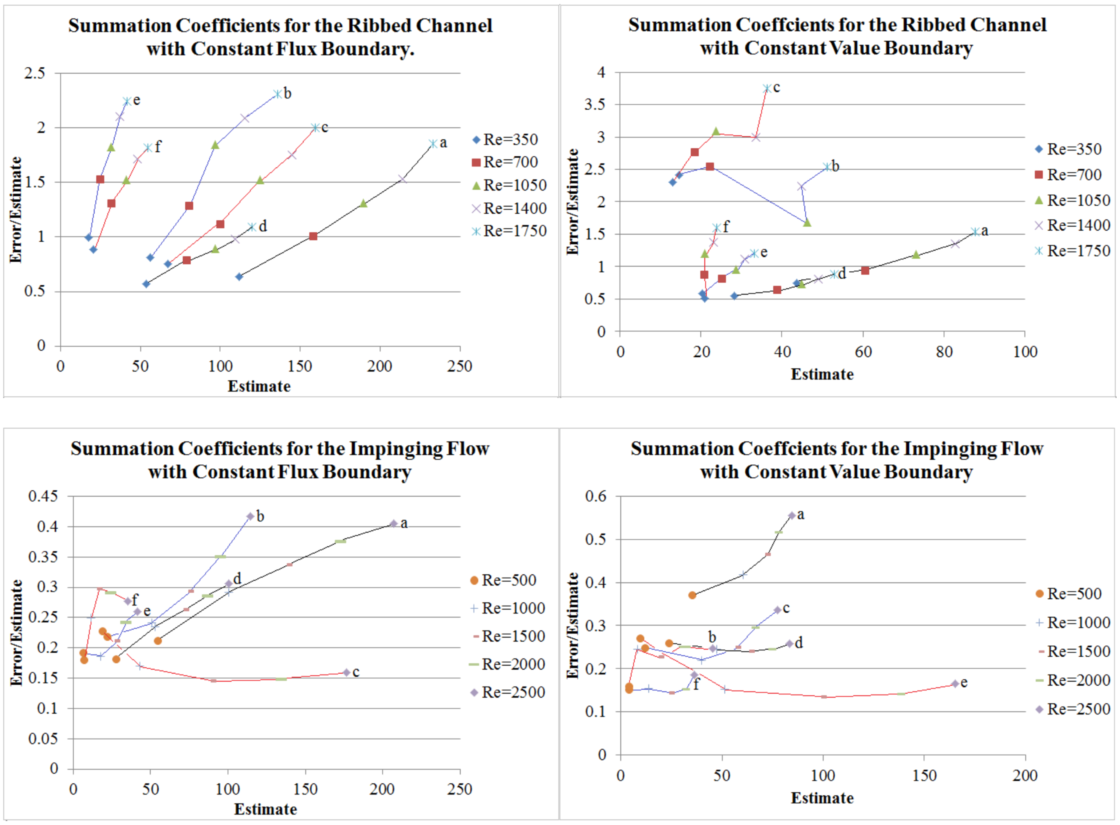

Figure 12: Plots of of the summation coefficients displayed as estimate against error divided by estimate. The simulations with the same discretisation schemes and mesh refinement have been joined by lines and labelled. The labels are: a - very coarse mesh with first order; b - very coarse mesh with second order centred; c - very coarse mesh with second order linear upwind; d - coarse mesh with first order; e - coarse mesh with second order centred; f - coarse mesh with second order linear upwind.

6.2.1 *Ribbed Channel Scale Prediction*

The scale of the error estimate for the ribbed channel tends to be a slight under-prediction, leading to ratios ranging from 0.5 to 3.5. Therefore the rescaling was successful at getting the error estimate to the same order as the real error. There are very clear and distinct lines visible in the graphs shown in Figure 12, showing that the scale of the estimate has a dependance on the discretisation scheme, the mesh refinement, and the Reynolds number. These lines are more clear for the ribbed channel results than for the impinging flow. The first order scheme produces the most consistent results, typically following a straight line with a shallow gradient. The second order results are not always so simple. Lines b and c in the ribbed channel results with constant value boundary are good examples of this. At high Reynolds number the data points diverge away from the expected trend line. This will be the effect of the increasing Peclet number and reaching a turbulent level of the Reynolds number causing the simulation of f and q to become less reliable. To get past this, introduction of a turbulence model is required.

The increasing summation coefficient ratio with Reynolds number might put another limit on the use of the method using a laminar simulation. If it continues the trend the ratio could become greater than an order of magnitude. However, the range of Re tested go into levels where there would normally be full turbulence, and the ratio did not pass 4. Beyond this Re, one would not be expected to be running a laminar simulation, so for test cases similar to these this would not be an issue. Another concern is that some of the lines go vertical, indicating the error is increasing while the estimate stays the same. An additional scaling factor that depends on Re may need to be included.

Figure 13 shows examples of the when the error estimate has over- or under-estimated the scale of the real error. In the over-estimation example the ratio is 0.57 and the source of the increased estimate is around the downstream rib. The prediction of the scale of the error elsewhere is at the same level as the real error values, for example behind the upstream rib both have a value of 90%. The under-estimation example shows a problem of the method when using a constant value boundary; the error estimation does not go towards zero at the 'hot' boundary, rather it increases sharply. The comparisons between f and q do not go to zero at the 'hot' boundary either which will affect the averaged quantities used for the rescaling process. This will affect the final scale and the summation coefficient and can cause the low summation estimate coefficients..

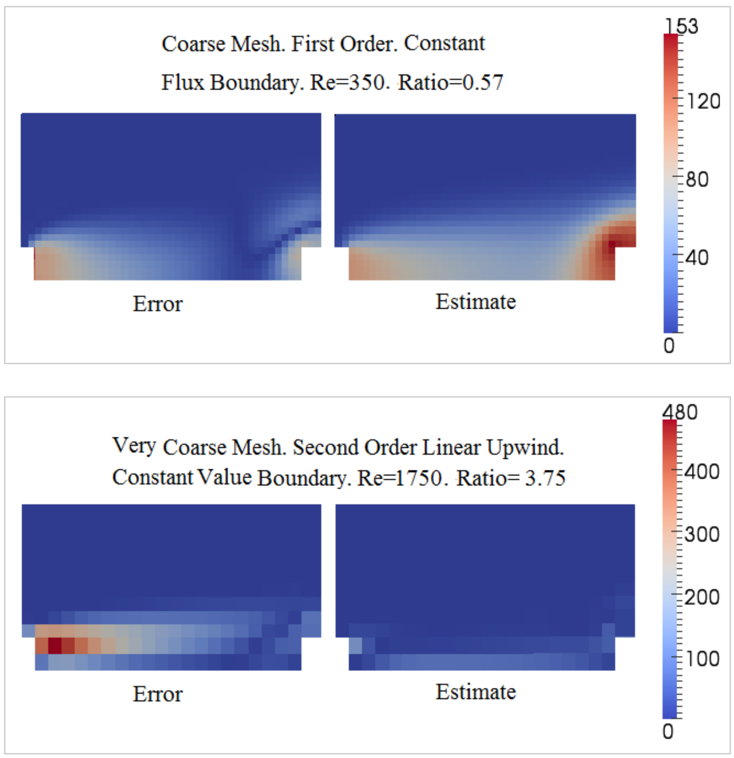

Figure 13: Comparison of the scale of the error estimate to the real error as a ratio summation error/estimate. On top is an example of an over-estimated scale with error/estimate=0.57. On the bottom is an example of an under estimated scale with error/estimate=3.75.

6.2.2 *Impinging Flow Scale Prediction*

In Figure 12 the ratios for the impinging flow case are consistently below zero, indicating an over-estimation of the scale of the error. From a practical point of view this is ideal so that the estimate serves as a reliable upper limit. The impinging flow results do not show lines that are as distinct as for the ribbed channel results. There are some that do obey a similar pattern as seen previously, for example lines a, b, and d from the constant flux boundary graph. Others do not, for example line f in the constant flux graph and line b in the constant value graph. They both increase between $Re = 500$ to 1500, then tail off or decrease as Re increases further.

Figure 14 shows two examples to demonstrate the scale prediction for the impinging flow. The first one is with the constant flux boundary with the second order linear upwind scheme with summation coefficient ratio 0.27. The error estimate has predicted the error at the impingment point successfully as well as the rest of the distribution except one difference. The real error has a line of zero error running through it that the estimate does not predict, leading to a smaller summation error. The maximum value of the error distribution is 65% at the impingement point and the maximum of the estimate is 71%. Therefore the estimate has successfully predicted the location where error can generate and to what level, only the summation coefficient masked the success

The first order constant value boundary result has an excellent match in shape, its correlation coefficient is 0.77. However, the estimate is an over-prediction of the distribution, with summation coefficient ratio 0.37. The cause of this is the rescaling of the estimate being too high.

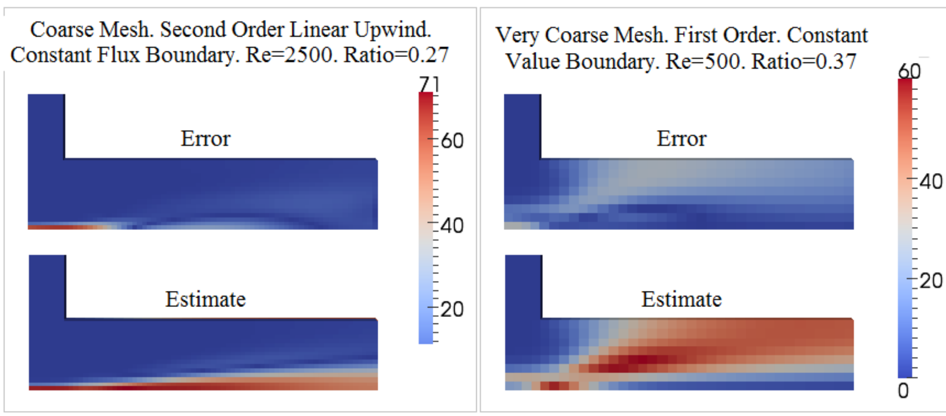

Figure 14: Comparison of the scale of the error estimate to the real error as a ratio summation error/estimate. Left is an example of a good scale prediction with a low ratio=0.27. Right is an example of good shape prediction with a low ratio=0.37.

7 Conclusions

There is a need in the CFD community for reliable, while efficient, methods to produce distributions of the simulation error. The objective of the work presented here was to create an error estimate that could meet the needs of industry and the CFD community. This error estimate would be based on a reliable method to predict the size and location of errors while at the same time not significantly increase the computer power and time taken to compute the CFD solution. An error estimate has been proposed: the second moment solution estimate (SMSE) based on the solving of a higher moment to compare to the first moment solution and reveal new information about the error. This uses only a single simulation in order to estimate the error. The drawback is that it requires the solving of an additional transport equation.

The method is expected to be quite powerful because the comparisons between the two solutions produce results that depend in large on the solution errors themselves. This paper reports on the use of two such comparisons, one for the shape and one for the scale. A deficiency of these is that the influence of the error from the second moment solution is significant, distorting the shape and changing the scale predictions. The error estimate was tested against two test cases that are complex enough to generate significant error and the results were compared using coefficients for the shape and scale.

The shape estimation was able to consistently predict the location of error from a simulation, and visually the predictions were very similar. Correlation coefficients ranged from 0.3 to 0.95 and the majority were above 0.7. It was also possible to rescale the shape estimate to the same order as the simulation errors. Judged using the summation coefficients, the estimate summation coefficient was consistently within a factor of four of the error summation coefficient. It was found that the SMSE consistently over-predicted the scale of the impinging flow errors, while in two thirds of the simulations it under-predicted the scale of the ribbed channel flow errors.

It was found that increasing *Re* leads to increasing the summation coefficient ratio. This means that *Re* would need to be taken into account to create a more accurate estimate. Another issue was that if the Peclet number is high then the possible unboundedness of the simulation can lead to a break down of the second moment solution, affecting the error estimate.

The SMSE performs better when applied to a constant flux boundary simulation, rather than a constant value boundary. Using a second order scheme, the constant value boundary condition leads to an error estimate with seemingly incorrect values at the 'hot' boundary. It was found to be non zero here, where it should be tending towards zero.

8 References

AIAA, AIAA Guide for the Verification and Validation of Computational Fluid Dynamics Simulations, AIAA 1998

Bird, R. et al, 'Transport phenomena,' Wiley, New York, 1962

Blottner, F. "Proceeding of the 3rd AIAA Computational Fluid Dynamics Conference", Albuquerque, New Mexico, published by AIAA 1977

Casey, M. and Wintergerste, T. "Best Practice Guidelines", ERCOFTAC Special Interest Group on "Quality and Trust in Industrial CFD" 2000

Fox, R. and McDonald, A. 'Introduction to fluid dynamics, vol. I,' Wiley, New York, 1982

Ferziger, J.H. and Perić, M. "Computational Methods of Fluid Dynamics" 3rd Ed., Springer 2002

Jasak, H. 'Error Analysis and Estimation for the Finite Volume Method with Applications to Fluid Flows' PhD thesis, Imperial College of Science, Technology and Medicine, 1996

Jasak, H. 'Automatic Resolution Control for the Finite-Volume Method, Part 1: A-Posteriori Error Estimates', Numerical Heat Transfer, Part B: Fundamentals: An International Journal of Computation and Methodology' 2010

Lemieux, L. and Barker, G. 'Measurement of small inter-scan fluctuations in voxel dimensions in magnetic resonance images using registration' Med. Phys. 25 1049–54,1998

Roache, P.J. "Verification and Validation in Computational Science and Engineering", Hermosa Publishers 1998

Rouse, H. et al., "History of Hydraulics", Dover Publications 1957

Wendt, J. F. "Computational Fluid Dynamics, An Introduction" 3rd Ed., Springer-Verlag Berlin Heidelberg 1992

Appendix A

Mathematical Analysis for Scalar Transport

This section will show why there is expected to be a difference between the two solutions. It breaks down the comparisons presented above and reveals what they represent in terms of the two solution errors. The solution errors need to be defined so that they can be used for the analysis. The error is the difference between the simulation solution and the exact solution. Therefore the error on the f simulation is

$$\delta = f - f_e \tag{28}$$

If the first moment produces a solution $f(= f_e + \delta)$, then after the source term is estimated the second moment equation becomes

$$\underline{u} \cdot \nabla q - \beta \nabla^2 q = -\beta \nabla (f_e + \delta) \cdot \nabla (f_e + \delta) \tag{29}$$

This can be expanded to give

$$\underline{u} \cdot \nabla q - \beta \nabla^2 q = -\beta \nabla f_e \cdot \nabla f_e - \beta \nabla \delta \cdot \nabla (2 f_e + \delta) \tag{30}$$

which after re-substituting for f_e using Equation 28 becomes

$$\underline{u} \cdot \nabla q - \beta \nabla^2 q = -\left[\beta \nabla f_e \cdot \nabla f_e\right] - \left[\beta \nabla \delta \cdot \nabla (2 f - \delta)\right] \tag{31}$$

where the source term has been split into the exact part which depends only on f_e and the discrepancy introduced by the incorrect $f\,(= f_e + \delta)$ solution. If the second term vanishes then this second moment equation would produce an estimation of q which would only have errors associated with the CFD procedure. The solving of this equation, with a non-zero second source part, produces a solution

$$q \quad = \quad q_e + \varepsilon \tag{32}$$

where ε represents all error associated with the q solution.

Now it can be seen what makes up the shape and scale combinations using these definitions. Using Equations 28 and 32 the shape estimate becomes

$$q - \frac{f^2}{2} = q_e + \varepsilon - \frac{(f_e + \delta)^2}{2} \tag{33}$$

This expands to give

$$q - \frac{f^2}{2} = q_e + \varepsilon - \frac{f_e^2}{2} - \frac{\delta\,(2 f_e + \delta)}{2} \tag{34}$$

which, after rearranging and cancelling the two exact parts, gives

$$q - \frac{f^2}{2} = \varepsilon - \delta \left(f - \frac{\delta}{2} \right) \tag{35}$$

Doing the same with the scale estimate, substituting the Equations 28 and 32 gives

$$f - \sqrt{2q} = (f_e + \delta) - \sqrt{2\,(q_e + \varepsilon)} - \tag{36}$$

which rearranges to become

$$f - \sqrt{2q} = f_e + \delta - \sqrt{2 q_e} \cdot \left(1 + \frac{\varepsilon}{2 q_e} \right)^{\frac{1}{2}} \tag{37}$$

Expanding the square root using a Taylor expansion gives

$$f - \sqrt{2q} \approx f_e + \delta - \sqrt{2 q_e} \left[1 + \frac{1}{2} \frac{\varepsilon}{2 q_e} - \frac{1}{8} \left(\frac{\varepsilon}{2 q_e} \right)^2 + \cdots \right] \tag{38}$$

and again the exact terms are cancelled and the result is

$$f - \sqrt{2q} \approx \delta - \frac{\varepsilon}{2 \sqrt{2 q_e}} + \frac{1}{8} \frac{\varepsilon^2}{2 q_e \sqrt{2 q_e}} - \cdots \tag{39}$$

Finally the $\sqrt{2q_e}$ can be substituted for f_e and the higher order terms dropped

$$f - \sqrt{2q} \approx \delta - \frac{\varepsilon}{2 f_e} \tag{40}$$

Appendix B

This section justifies the use of an additional factor of 2 in the estimate definition. The estimate without this additional factor and normalised to a percentage of a typical value of f would be

$$\frac{\left|q-\frac{f^2}{2}\right|\cdot\max\left(\left|\sqrt{2q}-f\right|\right)}{\max\left(\left|q-\frac{f^2}{2}\right|\right)}\frac{100\%}{\text{average}\,(f)} \tag{41}$$

Factorising the denominator gives

$$\frac{\left|q-\frac{f^2}{2}\right|\cdot\max\left(\left|\sqrt{2q}-f\right|\right)}{\max\left(\left|\frac{\left(\sqrt{2q}+f\right)\left(\sqrt{2q}-f\right)}{2}\right|\right)}\frac{100\%}{\text{average}\,(f)} \tag{42}$$

which if the approximation that $\max\left(\left|\left(\sqrt{2q}+f\right)\left(\sqrt{2q}-f\right)\right|\right)\approx\max\left(\left|\left(\sqrt{2q}+f\right)\right|\right)\max\left(\left|\left(\sqrt{2q}-f\right)\right|\right)$ the equation reveals a term in the numerator

$$\frac{\left|q-\frac{f^2}{2}\right|\cdot\max\left(\left|\sqrt{2q}-f\right|\right)}{\max\left(\left|\frac{\left(\sqrt{2q}+f\right)}{2}\right|\right)\max\left(\left|\left(\sqrt{2q}-f\right)\right|\right)}\frac{100\%}{\text{average}\,(f)} \tag{43}$$

Cancelling those two terms leaves

$$\frac{\left|q-\frac{f^2}{2}\right|}{\max\left(\left|\frac{\sqrt{2q}+f}{2}\right|\right)}\frac{100\%}{\text{average}\,(f)} \tag{44}$$

and using a second approximation that $\sqrt{2q}+f\approx 2f$ we find that the estimate is one term that is like $\frac{f^2}{2}$ divided by a term that is like f^2

$$\frac{\left|q-\frac{f^2}{2}\right|}{\max\left(|f|\right)}\frac{100\%}{\text{average}\,(f)} \tag{45}$$

Therefore multiplying by an additional factor of 2 will even this out.